JOURNAL OF MATERIALS SCIENCE **28** (1993) 423–439

Carbon fibre compressive strength and its dependence on structure and morphology

S. KUMAR
School of Textile and Fibre Engineering, Georgia Institute of Technology, Atlanta, GA 30332, USA

D. P. ANDERSON, A. S. CRASTO
University of Dayton Research Institute, Dayton, OH 45469, USA

The axial compressive strength of carbon fibres varies with the fibre tensile modulus and precursor material. While the development of tensile modulus and strength in carbon fibres has been the subject of numerous investigations, increasing attention is now being paid to the fibre and the composite compressive strength. In the present investigation, pitch- and PAN-based carbon fibres with wide-ranging moduli and compressive strengths were chosen for a study of fibre structure and morphology. A rayon-based carbon fibre was also included in this study. Structural parameters (L_c, $L_a(0)$, $L_a(90)$, orientation parameter Z, and the spacing between graphitic planes $d(0\,0,2)$) were determined from wide angle X-ray spectroscopy (WAXS). Fibre morphology was characterized using high-resolution scanning electron microscopy (HRSEM) of fractured fibre cross-sections. The mechanical properties of the fibres, including compressive strength, the structural parameters from WAXS, and the morphology determined from HRSEM are reported. The influence of structure and morphology on the fibre compressive strength is discussed. This study suggests that the width of the graphitic sheets, the crystallite size perpendicular to the fibre axis (L_c and $L_a(0)$), and crystal anisotropy play significant roles in accounting for the large differences in compressive strengths of various carbon fibres.

1. Introduction

The development of tensile modulus and strength in carbon fibres has been extensively studied over the past 30 years. A major application of these fibres is in structural composites where besides stiffness and tensile strength, other mechanical properties such as impact and compression strengths, and resistance to delamination are also important. The axial tensile stiffness and strength of unidirectional composites are primarily governed by the respective fibre properties, while resistance to impact loading and delamination depend on fibre, matrix, and their interface. Under compressive loading, composites of different carbon fibres with the same matrix and similar interlaminar shear strengths display a wide range of compressive strengths. These results reflect the influence of intrinsic fibre compressive strength on the corresponding composite property. In addition, matrix properties and the strength of the interfacial bond between fibre and matrix are also expected to influence composite compressive strength. In the recent past a number of studies has been conducted to understand the compression behaviour of fibres in the composite [1–10]. This list of references is by no means complete, and a significantly large number of publications have appeared in the literature on this subject in the last decade. The present study is an attempt to identify the structural and morphological factors that govern the compressive strength of carbon fibres.

A study on the fracture behaviour of carbon fibres by DaSilva and Johnson [11] concluded that the fracture morphology of PAN-based carbon fibres was different in tension and in flexure failure modes, while little difference was observed in the two fracture failure modes of the mesophase pitch-based carbon fibres. Loop behaviour of carbon fibres has been studied by several workers [12–15]. Jones and Johnson [12] observed that the carbon fibres heat treated to higher temperatures exhibited non-Hookean behaviour and this was attributed to the high compressive force in bending. A similar conclusion for carbon fibres was arrived at by Williams *et al.* [13], where loop stress–strain experiments were also performed on a strand of stainless steel wire and on quartz fibre, for comparison with carbon fibre.

From axial compression tests on unidirectional composites of pitch-based carbon fibres, it was observed that composites deform with strong reversible softening and that the softening increases with fibre modulus [16]. In another study, the non-linear behaviour was reported on single pitch- and PAN-based carbon fibres in tension and reversible softening of their unidirectional composites in compression [17]. The non-linearity was more pronounced in pitch-based fibres than in PAN-based fibres. In comparison, S-glass fibre and its unidirectional composite exhibited linear behaviour in tension and compression, respectively [17].

TABLE I Properties of various carbon fibres

	Tensile modulus (GPa)	Tensile strength (GPa)	Compressive strength (GPa)	Density ($g cm^{-3}$)	Typical fibre cross-section (μm^2)
Pitch-based					
Pitch-1					
P-25[a]	159	1.38	1.15	1.9	95
P-55[a]	379	1.72	0.85	2.0	82
P-75[a]	517	2.07	0.69	2.04	90
P-100[a]	724	2.24	0.48	2.15	88
P-120[a]	827	2.24	0.45	2.18	78
Pitch-2					
E-35[b]	241	2.83	1.26	2.10	88
E-75[b]	517	3.10	0.81	2.16	80
E-105[b]	724	3.31	0.74	2.17	80
K-135[c]	510	2.3	0.82	2.11	
PAN-based					
PAN-1					
T-300[a]	231	3.24	2.88	1.79	38
T-40[a]	290	5.60	2.76	1.78	24
T-50[a]	393	2.41	1.61	1.81	39
GY-70[d]	517	1.86	1.06	1.96	55
AS-4[e]	231	3.64	2.69	1.80	42
PAN-2					
M40J[f]	390	4.40	2.33	1.77	
M60J[f]	590	3.80	1.67	1.94	20
IM8[e]	310	5.17	3.22	1.80	24
Rayon-based					
T-75	538	2.62	1.03	1.80	

[a] Amoco fibres
[b] DuPont fibres
[c] Mitsubishi dialead fibre
[d] BASF fibre
[e] Hercules fibres
[f] Toray fibres.

The transverse fibre compressive strength of aramid fibres and of pitch- and PAN-based carbon fibres was recently measured by Kawabata [18]. As observed in axial compression, the transverse compression of highly oriented organic fibres showed ductile behaviour, while carbon and ceramic fibres exhibited brittle behaviour.

High-resolution scanning electron microscopy (HRSEM) of carbon fibres was reported by Vezie and Adams [19], where a particulate structure was observed in the PAN-based AS-4, T-300, and T-40 carbon fibres. Well-developed sheet-like structure was observed in most mesophase pitch-based carbon-fibres and PAN-based GY-70. Some development of sheet-like character was also observed in PAN-based T-50 fibre. The structure of several pitch-based carbon fibres was also studied by wide-angle X-ray scattering (WAXS), electron microscopy, and transverse magnetoresistance [20]. From this study it was suggested that the folded sheet structure contribute so to the lower graphitizability of the fibres.

With boron-ion implantation, the carbon fibre compressive strength and torsional modulus increased by up to 25% and 50%, respectively, while the crystallite size, L_c, decreased [10]. An improvement in shear resistance was considered responsible for the increased compressive and torsional properties. A correlation between torsional modulus and compressive strength was reported for a broad range of fibres including polyethylene, Kevlar™, pitch- and PAN-based carbon, glass, boron, and alumina fibres [5]. The compressive strength of composites reinforced with T-300 and T-800 carbon fibres decreased with increasing test temperature [21]. This is mainly due to the decrease in resin modulus with temperature increase and hence reduced lateral support against fibre buckling. The composite compressive strength of the higher modulus and low compressive strength pitch-based P-100 fibre did not change that significantly in this temperature range [22]. Thermodynamic analysis of kinking in composites has been performed by Evans and Adler [23] with the conclusion that the matrix yield strength plays a central role in kink suppression.

A number of pitch- and PAN-based carbon fibres, and one rayon-based carbon fibre were selected for this study. Fibres and their tensile properties as reported by the manufacturers, are listed in Table I. Typical fibre cross-sectional areas of these fibres as measured by laser diffraction are also listed. The fibre compressive strength values are also reported in Table I, and these were determined from the composite compressive strength by normalizing to 100% fibre. Axial composite compression strengths were obtained from the literature [1, 9, 24]. The high-modulus carbon fibre composites (e.g. P-75 and P-100) fail in the shear mode [4], while the high compressive strength carbon fibre composites (e.g. T-300) fail in the buckling mode. Therefore, the compressive strength of the latter fibres, reported in Table I, represent the lower limit of fibre compressive strength. Higher compressive strength values for some of these fibres are predicted from various single fibre tests. Assumptions involved in these various tests, however, make it difficult to unequivocally measure the compressive strength of carbon fibres (refer to discussion and references cited in [1], and [25–30]). Therefore, the data have been taken from composite tests, with the reservation that the compressive strength values of fibres such as T-300, AS-4, T-40, and IM-8, may be underestimated.

Carbon fibre compressive strength as a function of tensile modulus is plotted in Fig. 1. From this figure it is evident that the carbon fibre compressive strength decreases with increase in modulus, and that for a given modulus the compressive strengths of PAN-based carbon fibres are higher than those of the pitch-based fibres. However, for both pitch and PAN, the same modulus fibres can have different compressive strengths. The very high modulus pitch-based carbon fibres have the lowest compressive strength. The compressive strength of rayon-based carbon fibres (Table I) is also low. In Fig. 1, the PAN-based carbon fibres have been divided into two categories; PAN-1 and PAN-2. For the same fibre modulus, the PAN-2 fibres have higher compressive strength than the PAN-1 fibres. Similarly, the pitch-based carbon fibres have been divided into pitch-1 and pitch-2, where pitch-2 fibres have slightly higher compressive strength than the pitch-1 fibres for the same fibre modulus. This scheme of categorization of pitch- and PAN-based carbon fibres has been used throughout the paper.

By comparison, the compressive strengths of all polymeric fibres are low, and Kevlar, with an axial compressive strength of approximately 450 MPa, is the highest compressive strength polymeric fibre. The compressive strength of bulk polymers is also lower than that of Kevlar; PBI resin has a compressive strength of about 400 MPa, while the compressive strengths of the common thermoplastic and thermosetting resins are in the range 100–250 MPa. On the other hand, fibres of materials such as Al_2O_3 and boron have high compressive strengths, and this is of the order of 5–7 GPa. The compressive strength of carbon fibres falls in between the compressive strengths of these two classes (polymeric and inorganic fibres). The compressive strength of bulk ceramics and oxides is generally low, presumably due to flaws [1, 31].

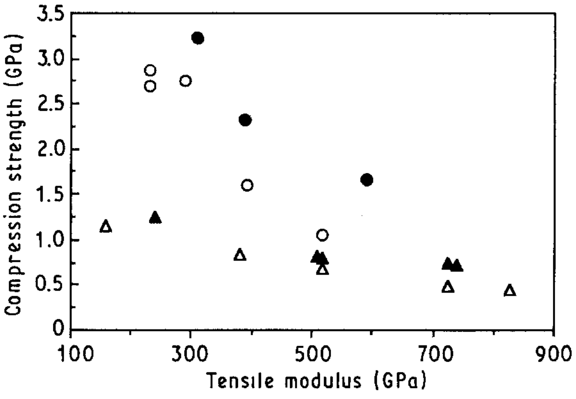

Figure 1 Carbon fibre compressive strength as a function of fibre tensile modulus. (△) Pitch-1, (▲) pitch-2, (○) PAN-1, (●) PAN-2.

In a recent study [5] of a number of different fibres it was shown that, with some exceptions, the fibre compressive strength increased with decreased fibre anisotropy, where fibre anisotropy was defined as the ratio of the fibre tensile modulus, E, to the fibre shear-modulus, G. Considering that certain defects and morphological features which influence the tensile strength, TS, may also affect the compressive strength, the compressive strength was plotted as a function of $TS/(E/G)$ for a number of PAN-based fibres. The good correlation observed suggests that the fibre anisotropy and the structural features or flaws governing the tensile strength influence the compressive strength [31]. However, this observation is only for fibres with limited variation in properties. The emphasis of the current work has been to look for features which can explain the compression behaviour of all types of carbon fibres with wide ranging properties,

Carbon fibres can be intercalated with a number of elements including halogens and alkali metals such as potassium, sodium and cesium. Herinckx *et al.* [32, 33] studied the intercalation of rayon-based carbon fibres. Carbon fibres have also been intercalated in oxygen and in nitric acid [34, 35]. A good review of the subject is given by Dresselhaus *et al.* [36]. Jaworske *et al.* [37, 38] intercalated pitch-based carbon fibres in the presence of bromine vapour, and evaluated the properties of the intercalated and pristine fibres in composites. Composites of bromine-intercalated P-75 and of pristine P-75 fibres were evaluated in compression [1]. The composite compressive strength, and hence fibre compressive strength, remained essentially unchanged with intercalation. Tensile strength and modulus also did not change with intercalation. A slight improvement was observed in interlaminar shear strength and attributed to the increased rugosity of the fibre surface due to the intercalation process. In the intercalated fibre bromine has only one-dimensional order and that is along the fibre axis. The periodicity of this order along the fibre axis as observed from the WAXS pattern is 0.415 nm [1]. In compression, the brominated fibre composite fails with axial fibre splitting [1, 39]. Because the intercalant goes in between the graphitic sheets it is expected to influence the intermolecular interaction between these sheets. However, because the compressive strength is essentially unaffected by bromine intercalation, this leads to one or both of the following conclusions: (i) bromine intercalation does not significantly affect the intermolecular interaction between the graphitic sheets, (ii) intermolecular interaction does not affect the compressive strength, at least in the high-modulus pitch-based carbon fibres. Whether both of these arguments are true is not currently known. Applications of the intercalated compounds are discussed by Inagaki [40]

2. Experimental procedure

Wide-angle X-ray scattering (WAXS) was performed

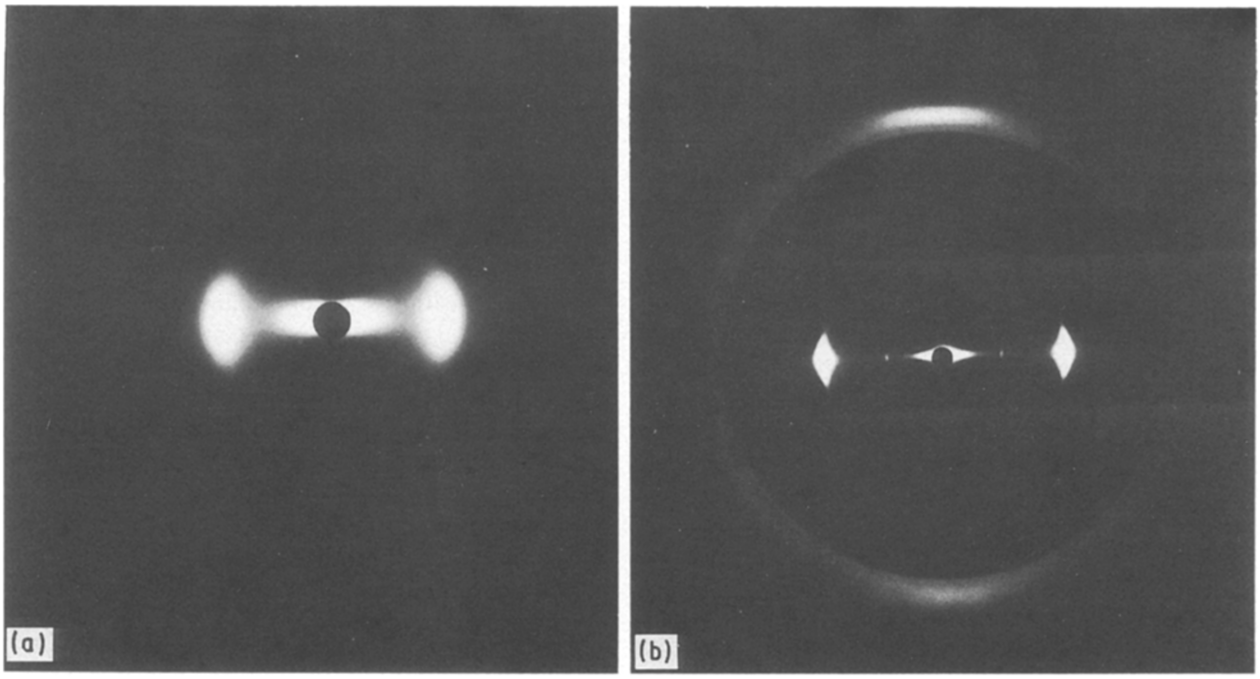

Figure 2 Flat film wide-angle X-ray scattering photographs of (a) P-100 and (b) T-300 carbon fibres.

on a four-circle X-ray diffractometer using CuK_α radiation from a Rigaku RU-200 rotating anode generator operated at 45 kV and 70 mA. For these experiments, fibre bundles were mounted on cardboard holders using a wicking glue. Radial scans were obtained at $\phi = 0°$, 70°, and 90° (where 0° and 90° scans correspond to equatorial and meridional scans respectively). The scan at 70° was selected to detect the presence of the three-dimensional reflections; (1 1, 2) and (1 0, 1). For the ideal orientation of graphite planes along the fibre axis, the maximum intensity of (1 1, 2) and (1 0, 1) planes should occur at 69.8° and at 72.4°, respectively. $\phi = 70°$ was chosen so that the presence of either reflection could be observed. Azimuthal scans were obtained for the (0 0, 2) reflection for determination of planar orientation. Typical wide-angle flat plate photographs of a pitch-based fibre (P-100) and PAN-based fibre (T-300) taken with a Statton–Warhus camera are shown in Fig. 2. The planes (1 1, 0) and (1 0, 0) on the graphitic sheets are shown in Fig. 3, and both planes are perpendicular to the plane of the paper.

Intensity data were fitted with Pearson Type VII profiles [41], and mis-centring of the fibre bundle in the diffractometer was corrected by averaging selected peak positions on the positive and negative Bragg angle scans. Intensities were also corrected for absorption, polarization, and air scattering. Corrections for the Lorentz and structure factors were also made. The Lorentz correction factor for an equatorial plane is given by [42]

$$L(h\,k, l) \;=\; (\sin^2\theta \cos\theta)^{-1} \qquad (1)$$

where θ is the Bragg angle. The structure correction factor for the $(h\,k, l)$ reflection, in a crystal with n atoms per unit cell is given by

$$F\,(h\,k, l) \;= \sum_n \left[f_n \exp\left\{2\pi \mathrm{i}(hx_n + ky_n + lz_n)\right\}\right] \qquad (2)$$

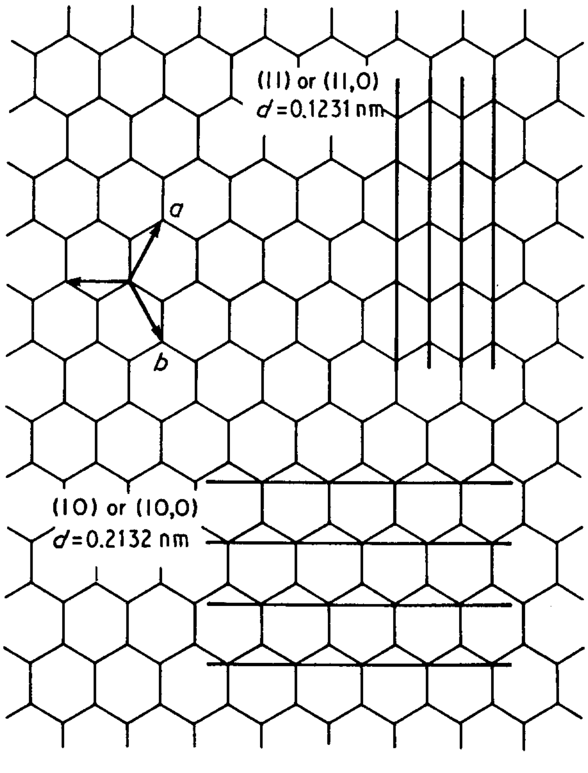

Figure 3 Graphite sheet showing (1 1, 0) and (1 0, 0) plane.

where f_n is the atomic scattering factor for the nth atom, and x_n, y_n, and z_n represent the coordinates of that atom in the unit cell. For equatorial reflection (0 0, 1) in carbon fibres, the structure factor F (0 0, 1) is a constant times the atomic scattering factor of carbon. The Lorentz and structure correction factors for carbon fibres in the 2θ range of (0 0, 2) are plotted in Fig. 4 as a function of Bragg angle. This figure also shows the uncorrected and corrected (0 0, 2) plots of P-25 and P-100 carbon fibres. P-25 fibre, with a very broad (0 0, 2) reflection, shows a significant shift in the peak position when Lorentz and structure correction

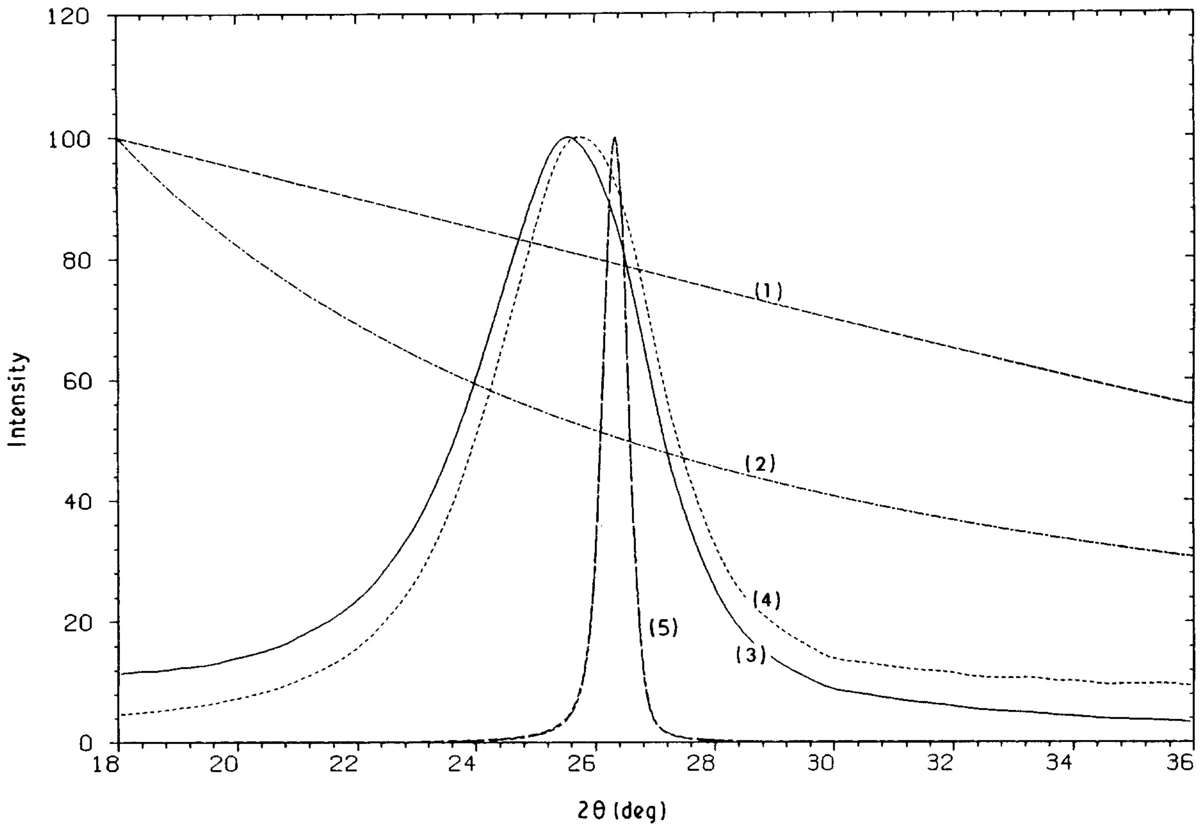

Figure 4 Structure factor (1) and Lorentz correction factor (2) as a function of 2θ. Radial scans of P-25 (3, uncorrected, and 4, corrected for structure and Lorentz correction factors) and of P-100 (5, corrected and uncorrected) fibre at $\phi = 0$ in the 2θ region of (0 0, 2).

factors are applied, while the P-100 fibre with a relatively narrow peak does not show a discernible shift. The structure and Lorentz correction factors were applied to the (0 0 2) equatorial scans only, so that d(0 0 2) could be accurately determined.

The crystallite size, L_c, was calculated using the Scherrer equation [43]

$$L_c = K\lambda/(\beta\cos\theta) \qquad (3)$$

where $(\beta)^2 = (\beta_0)^2 - (\beta_i)^2$. β_0 is the experimentally observed integral breadth in 2θ radians. The subscript i indicates instrumental contribution to the broadening. The broadening contribution due to finite sample size was neglected. The instrumental line broadening was determined using hexamethylene tetramine crystals, which were so large, that essentially all the observed broadening for these crystals could be assumed to arise due to instrumental effects. The above correction equation also assumes that both the instrumental broadening profile and the specimen profiles have Gaussian distributions. The instrumental profiles were, in fact, Gaussian, whereas the sample profiles were not always so. However, the sample profiles approached a Gaussian distribution as the breadth narrowed, where the corrections are most critical. The Scherrer analysis [43] was chosen over more sophisticated analyses [44–46] as the latter involved significantly more work without additional benefit. L_a was determined from (1 0, 0) and (1 1, 0) reflections from 0°, 70°, and 90° radial scans using Ruland's equation for two-dimensional crystals [47, 48], which is a simplification of a previous analysis [49, 50]

$$L = 1.84\,\lambda/[B_{(1/2,\,2\theta)}\cos\theta] \qquad (4)$$

where $B_{(1/2,\,2\theta)}$ is the full-width at half-maximum. The intensity profiles of (1 0, 0) and (1 1, 0) are asymmetric, and the value of $B_{(1/2,\,2\theta)}$ was determined from these asymmetric profiles.

For microstructural examination, the fibres were fractured in bending by tying a knot in a strand of fibres and closing the loop. Cross-sections of fibres fractured in this manner were observed uncoated in a Hitachi S-900 high-resolution scanning electron microscope (HRSEM), at an operating voltage of 1–2 kV. The Hitachi S-900 is a field-emission gun scanning electron microscope with a high-intensity electron source at low voltages, capable of providing excellent resolution down to a few nanometres.

3. Results and discussion

3.1. Wide-angle X-ray scattering

The various structural parameters determined from WAXS are L_c, $L_a(0)$, $L_a(90)$, d(0 0, 2), and Z, and the extent of three-dimensional order, where L_c is the crystallite size perpendicular to graphitic sheet, $L_a(0)$ and $L_a(90)$ are the crystallite sizes along the graphitic sheet perpendicular and parallel to the fibre axis and, obtained from equatorial ($\phi = 0°$) and meridional ($\phi = 90°$) scans, respectively. Because radial scans were also taken at $\phi = 70°$, $L_a(70)$ is also measured, d(0 0, 2) is the d-spacing between graphitic planes, and Z is the full-width at half-maximum of the (0 0, 2) azimuthal scan in degrees.

The 2θ angular dependence of the Lorentz and structure correction factors and the uncorrected and corrected intensity profiles of the (0 0, 2) reflections for

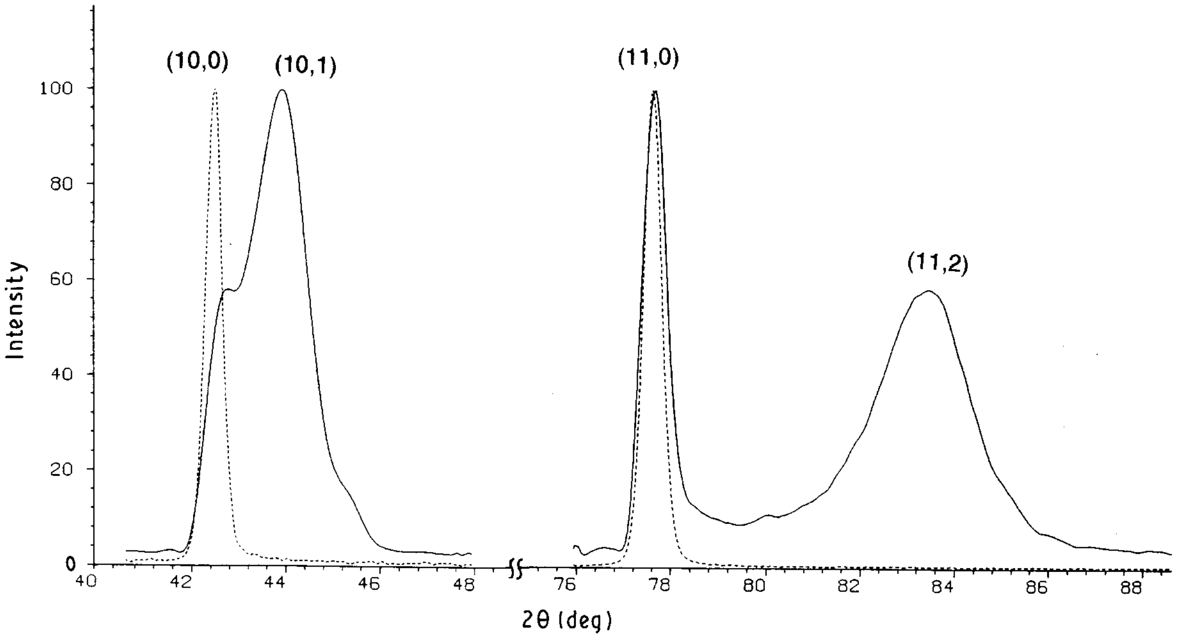

Figure 5 Radial scans of P-100 fibre at ϕ = (——) 70 ° and (- - -) 90 ° in the 2θ range of (1 0, 0), (1 0, 1), (1 1, 0), and (1 1, 2) reflections.

P-25 and P-100 fibres are shown in Fig. 4. When the correction factors are applied, a significant shift is observed in the position of the P-25 peak, while the peak position of P-100 fibre remains essentially unchanged. The peak positions of specimens with small crystallite sizes are significantly more sensitive to the Lorentz and structure factor corrections. These corrections result in smaller *d*-spacings, and the corrected *d*-spacings are reported in Table II. Relatively larger *d*-spacings reported earlier [1] were calculated without the application of these corrections. Northolt and Stuut [51] described this method as a means of correcting the intensity profiles for crystal size effects and angular dependence of the structure and Lorentz factor corrections.

The (0 0, 2) *d*-spacings of the pitch-2 fibres are higher than the corresponding *d*-spacings of the pitch-1 fibres of the same modulus. Similarly the *d*-spacings of PAN-2 fibres are slightly higher than those of PAN-1 fibres of the same modulus. The two fibres in common between this study and that of Endo [20] are P-100 and P-120, and the *d*-spacings and the L_c values in the two studies are comparable. Endo reported *d*-spacings of 0.3392 and 0.3378 nm and L_c of 24 and 28 nm for P-100 and P-120 fibres, respectively, and no mention was made of the Lorentz and structure correction factors. The corresponding values in our study are: 0.3382, 0.3376, 22.7 and 25.1 nm. The small differences in *d*-spacings in two studies may be due to the application of correction factors in the present study. Another point worth noting here is that Endo's work was done on powdered fibre samples, while the present work was performed on the fibre bundles. The comparison of the crystallite sizes from the two studies suggests that the crystallites remain essentially unaffected in the powdering process.

The radial scans of P-100 fibre at ϕ of 70° and 90° (meridional) are given in Fig. 5. In the meridional scan ($\phi = 90°$) the reflections (1 0, 1) and (1 1, 2), indicative of three-dimensional order, are absent. The intensity of these reflections is very strong, however, in scans at $\phi = 70°$, demostrating the necessity of such scans. An alternative to this approach is the powdering process as used by Endo [20], where all orientations are averaged out, and only one radial scan is used to observe all reflections. The use of a fibre bundle was favoured, however, so that the orientation parameter could also be determined from the same sample, and L_a could be measured along and perpendicular to the fibre axis. Radial scans at $\phi = 70°$ of several pitch-based and PAN-based fibres in the 2θ range of the (1 0, 0), (1 0, 1), (1 1, 0), and (1 1,2) reflections are given in Figs. 6–8. Fibres which demonstrate a peak for the (1 0, 1) reflection and/or the (1 1, 2) reflection in the 70° scan are considered to have three-dimensional order; those with only a mild shoulder in the intensity profile have partial development of three-dimensional order. A fibre with only an asymmetric intensity distribution in the 2θ range of (1 1, 0) and (1 0, 0) reflections is considered to have only two-dimensional order. On this basis, from Figs 5–8, one can say that P-100, P-75, GY-70, and M60J appear to have well-developed three-dimensional order, while in P-55 and T-50, which have a shoulder in the intensity profile, the three-dimensional order is beginning to develop. The categorization of all the fibres in this manner is indicated in Table II.

The L_c values obtained from the (0 0, 2) reflection are reported in Table II. The L_a values perpendicular, parallel, and at 70° to the fibre axis were determined by taking the average of the corresponding L_a values from the (1 0, 0) and (1 1, 0) reflections. The L_a values from individual reflections and their averages are listed in Table III. Only the average values are considered in further discussion.

The development of various crystalline and orientation parameters is not independent of each other, and this is clearly demonstrated in Figs 9–11. In Figs 9 and 10, L_c is plotted as a function of the orientation parameter, Z, and crystallite size, $L_a(0)$, respectively. Fig. 9

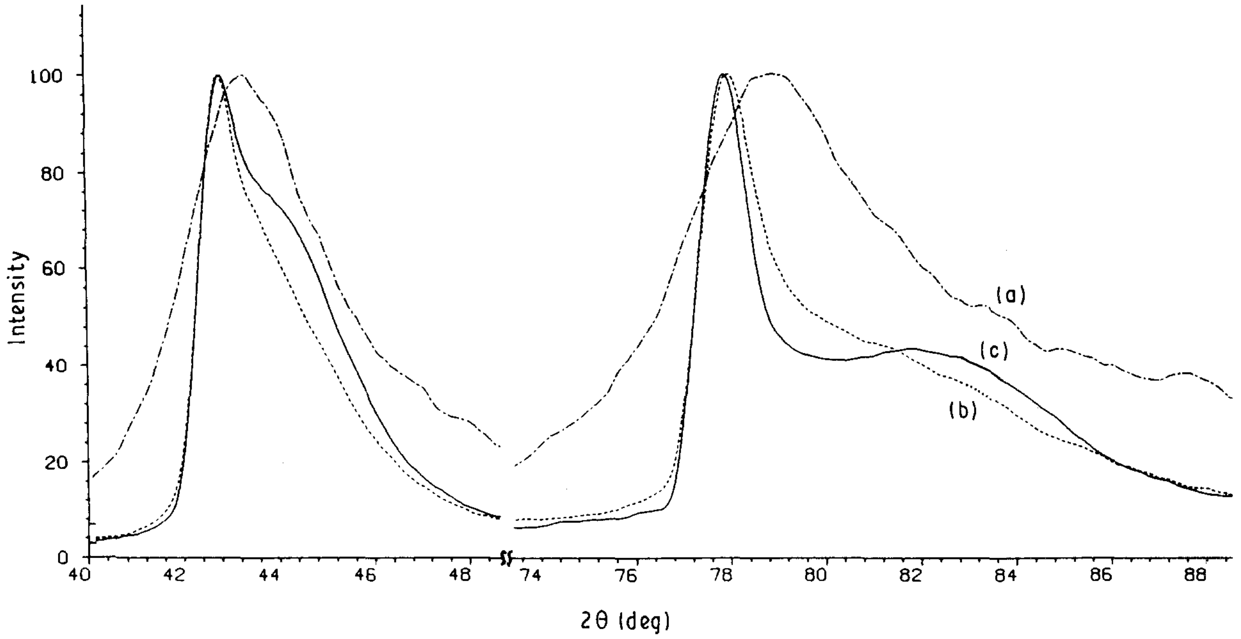

Figure 6 Radial scans of (a) P-25, (b) P-55, and (c) P-75 fibres at $\phi = 70°$.

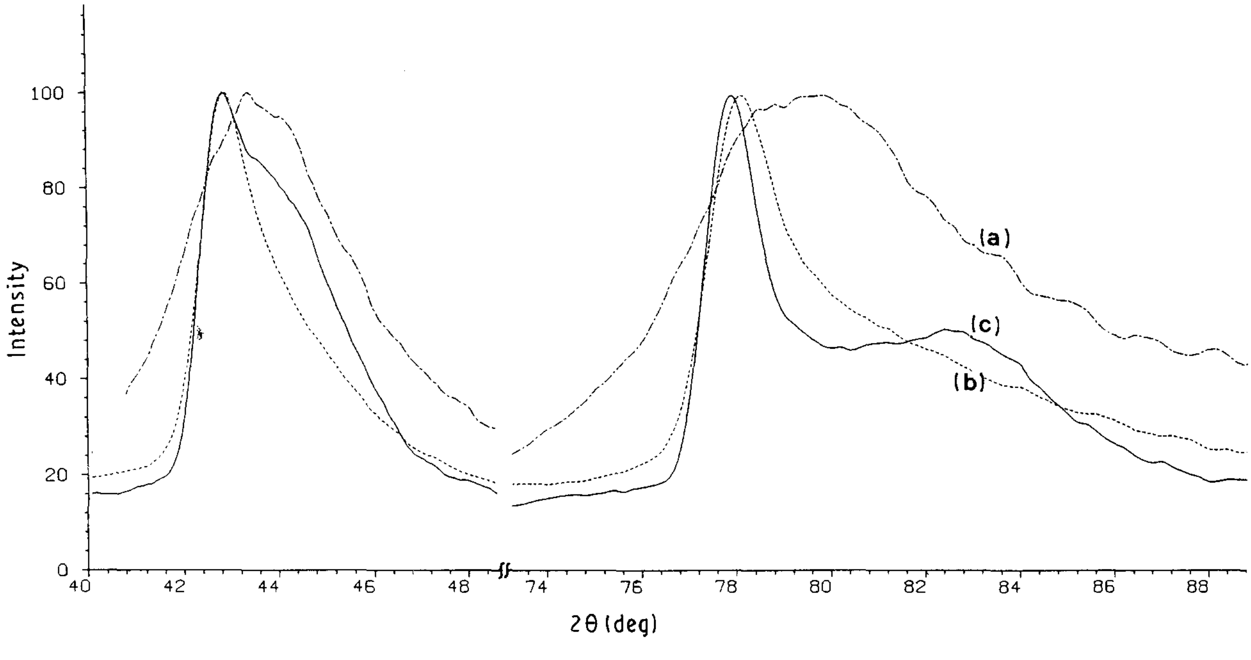

Figure 7 Radial scans of PAN based (a) T-300, (b) T-50, and (c) GY-70 fibres at $\phi = 70°$.

indicates that an increase in crystallite orientation is accompanied by an increase in crystallite size perpendicular to the graphitic planes. The crystallite sizes of the pitch-2 fibres are lower than those of the pitch-1 fibres of the same orientation. Fig. 10 indicates that for fibres of crystallite size below 20 nm, the values of $L_a(0)$ and L_c are about the same. P-100 and P-120 fibres with larger crystallite sizes have an $L_a(0)$ value almost twice that of L_c. The difference between $L_a(0)$ and L_c in a pitch-2 fibre of similar modulus, E-105, is not as large. The larger values of $L_a(0)$ in P-100 and P-120 may suggest a greater degree of sheet straightening along the fibre axis in these fibres. From Fig. 11 it appears that for $L_a(0)$ less than 20 nm, the value of $L_a(90)$ is almost double that of $L_a(0)$. On going from P-100 to P-120, there is a larger increase in $L_a(0)$ than in $L_a(90)$, even though the absolute value of $L_a(90)$ is still larger than that of $L_a(0)$ for these two fibres. Because $L_a(90)$ is a measurement along the fibre axis (along the length of the fibrils), the larger values of $L_a(90)$ as compared to $L_a(0)$ are not surprising. For the same modulus pitch-1 and PAN-1 fibres, all the crystallite dimensions are, in general, larger than those of the pitch-2 and PAN-2 fibres, respectively.

3.2. Morphology

Scanning electron micrographs of the transverse cross-sections of varous pitch- and PAN-based carbon fibres are shown in Figs 12–18. For comparison, the scanning electron micrographs of E-glass fibre cross-section are shown in Fig. 19. Fig. 12 shows views

TABLE II Structural parameters of various carbon fibres

Fibre	L_c (nm)	Z (deg)	$d(0\,0,2)$ (nm)	Three-dimensional order	SEM morphology	Nitrogen content (%)
Pitch-1						
P-25	2.6	31.9	0.344	No	Sheet-like	
P-55	12.4	14.1	0.342	May be		
P-75	14.6	11.0	0.3410	Yes	Sheet-like	
P-100	22.7	5.6	0.3382	Yes	Sheet-like	
P-120	25.1	5.6	0.3376	Yes	Sheet-like	
Pitch-2						
E-35	3.2	21.6	0.344	No		
E-75	10.3	10.9	0.3424	Yes		
E-105	13.8	7.2	0.3420	Yes		
K-135	11.9	10.4	0.3422	Yes		
PAN-1						
T-300	1.5	35.1	0.342	No	Particles	8.5%
T-40	1.8	30.2	0.343	No	Particles	3.8%
T-50	5.3	16.4	0.3423	May be	Some sheet-like Character obs.	0.05%
GY-70	14.1	9.6	0.3396	Yes	Sheet-like	0
AS-4	1.8	36.8	0.342	No	Particles	
PAN-2						
M40J	3.6	21.4	0.3427	No		0
M60J	7.8	9.9	0.3411	Yes	Particles	0
IM8	1.9		0.3431	No		
Rayon-based						
T-75	8.4	8.7	0.3403	Yes		

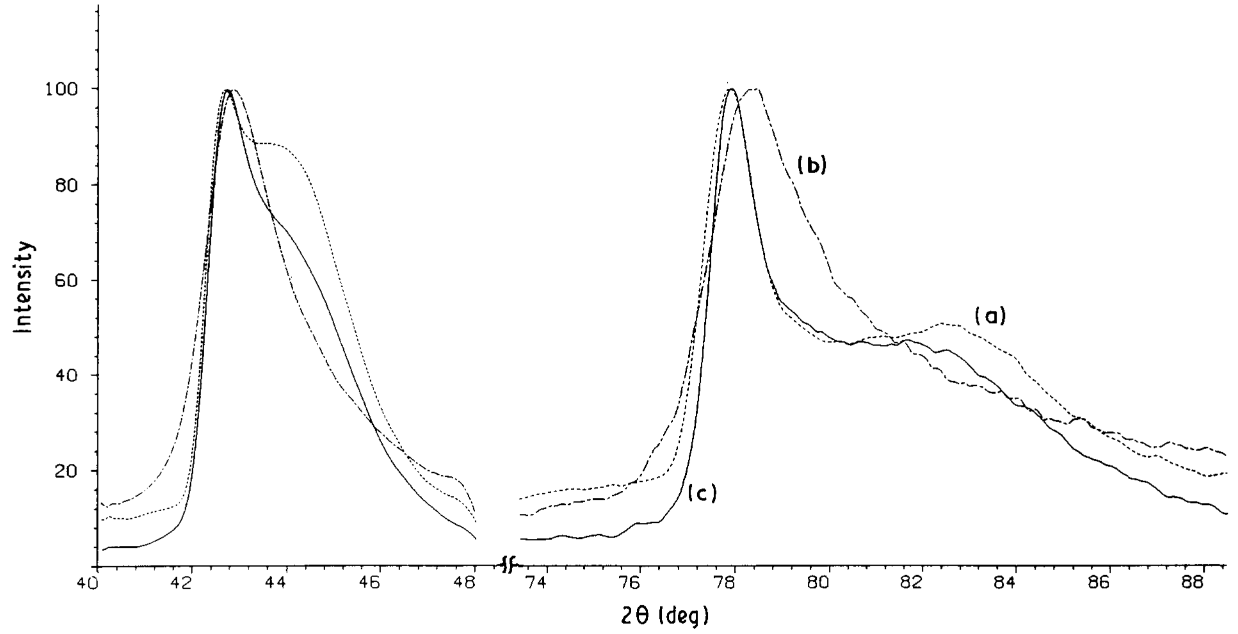

Figure 8 Radial scans of (a) GY-70, (b) M40J, and (c) M60J at $\phi = 70°$.

of P-25 fibre at low and high magnification. Even though P-25 has a low modulus, relatively low density, and the absence of three-dimensional order, the micrographs indicate sheet-like order. The thickness of the sheets appears to be of the order of 15 nm and the width is much larger. From WAXS measurements, L_c for this fibre is 2.6 nm, and $L_a(0)$ and $L_a(90)$ are 4 and 6 nm, respectively. The sheet thickness determined from HRSEM micrographs is significantly larger than L_c, and this is probably due to the lack of graphitic order within the sheets. With increasing fibre heat treatment this waviness is ironed out, as seen in the higher modulus P-100 fibre (Fig. 13). The low-magnification micrograph of P-100 fibre indicates the well-developed sheet-like morphology, and this microstructure is similar to that reported by Endo [20] for P-120 fibre. High-resolution images of transverse and longitudinal sections of P-100 fibre at higher magnification are shown in Figs 13b and c. From Fig. 13b, the sheet thickness is seen to be approximately 25 nm. The measured value of L_c for this fibre from WAXS is 22.7 nm. The excellent agreement between the sheet thickness from HRSEM andL_c from WAXS indicates that direct dimensional measurement of the well-formed graphitic sheets is possible using HRSEM. Measurement of the width of the graphitic sheets is

TABLE III L_a (nm) values obtained from different reflections

	$L_a(0)$			$L_a(70)$			$L_a(90)$		
	(1 0,0)	(1 1,0)	Average	(1 0,0)	(1 1,0)	Average	(1 0,0)	(1 1,0)	Average
Pitch-1									
P-25	5	3	4	5	4	4.5	7	5	6
P-55	11	12	11	12	16	14	31	28	29.5
P-75	10	17	13	4	17	10.5	26	28	27
P-100	–	49	49	–	56	56	85	75	80
P-120	–	64	64	–	70	70	78	97	88
Pitch-2									
E-35	5	–	5	6	4	5	8	6	7
E-75	13	14	13	9	10	9.5	24	20	22
E-105	13	21	17	–	14	14	34	30	32
K-135	13	13	13	–	12	12	28	24	26
PAN-1									
T-300	–	2.2	2.2	4.3	3.7	4	4.6	3.6	4.1
T-40	3.7	2.3	3.0	4.4	3.4	3.9	5.4	3.8	4.6
T-50	7.9	4.9	6.5	9.1	8.9	9	18	17	17.5
GY-70	9	15	12	–	25	25	37	43	40
AS-4	3.7	2.3	3	4.8	3.5	4.1	4.4	3.6	4.0
PAN-2									
M40J	6.6	4.5	5.5	9.3	7	8.1	14	11	12.5
M60J	8	6.4	7	–	14	14	29	28	28
IM8	3.5	2.7	3.1	5.7	4.1	4.9	5.6	4,6	5.1
Rayon									
T-75	10	9	9.5	–	17	17	37	35	36

[a] L_a average is calculated from (1 0 0) and (1 1 0).

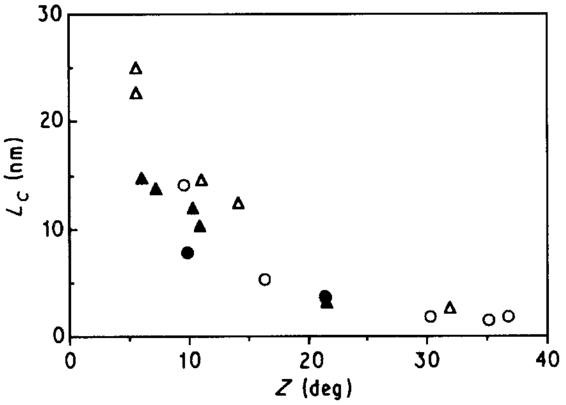

Figure 9 Plot of L_c as a function of full-width at half-maximum, Z, of the azimuthal scan of the (0 0, 2) reflection. (△) pitch-1, (▲) pitch-2, (○) PAN-1, (●) PAN-2.

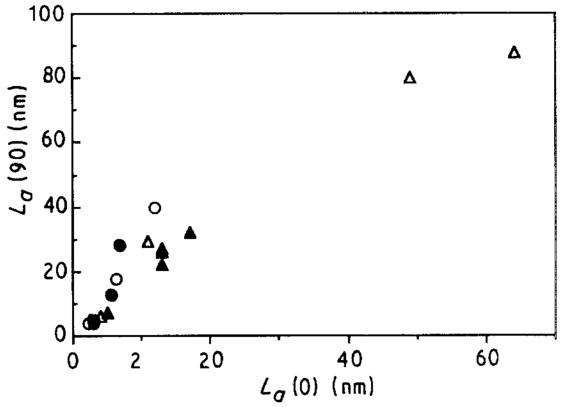

Figure 11 Plot of L_a (90) (crystal size parallel to the fibre axis) as a function of L_a (0) (crystal size perpendicular to the fibre axis). For key, see Fig. 9.

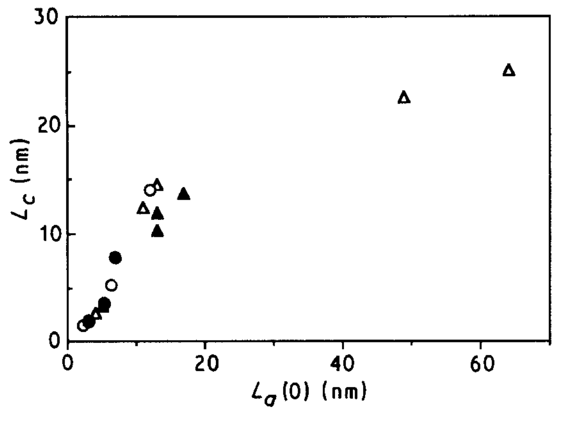

Figure 10 Plot of L_c as function of $L_a(0)$. For key, see Fig. 9.

not as straight forward, as a large variation is observed in this dimension. This variation arises mainly because the distinction between two different sheets is not always clear. However, from the micrographs it is seen that the width of the sheets in P-100 is greater than 500 nm. The $L_a(0)$ value for this fibre from WAXS is 49 nm, indicating at least an order of magnitude difference between the WAXS measurement and direct measurement from HRSEM. However, this apparent discrepancy between the two measurements is not surprising, as bends in the graphitic sheets and waviness along the width limits the $L_a(0)$ measurement from WAXS. Similarly, the sheet dimension along the fibre axis could be an order of magnitude or more greater than $L_a(90)$ measured from WAXS. The

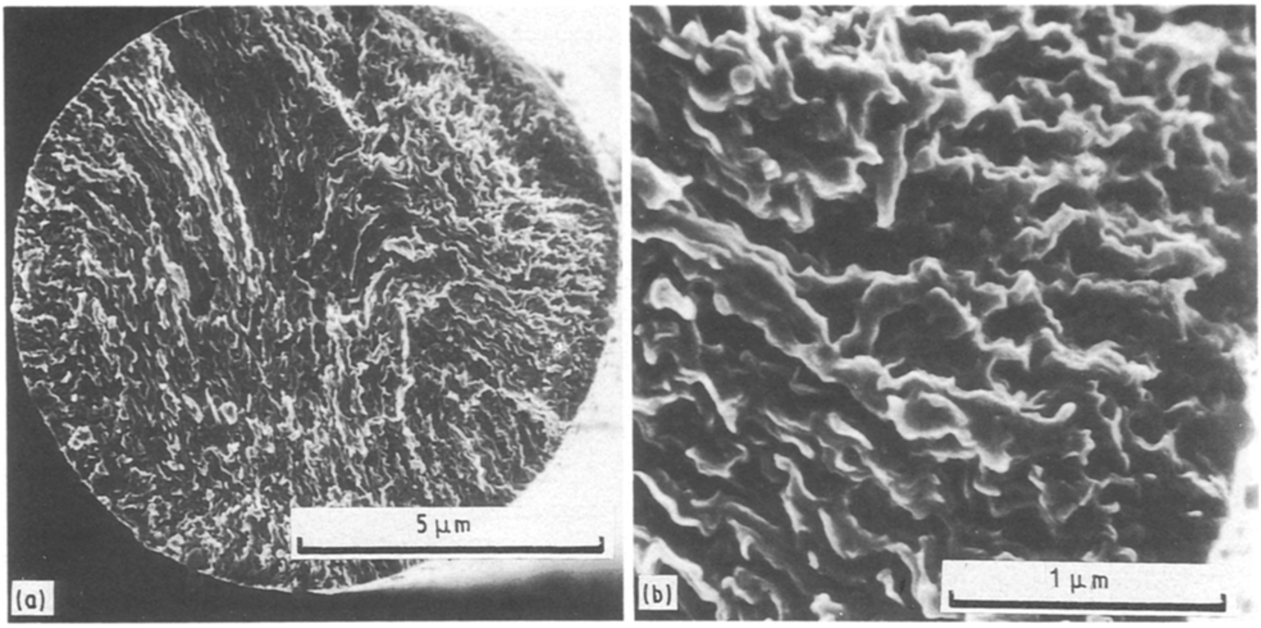

Figure 12 Scanning electron micrographs of pitch-based P-25 fibre at low (a) and high (b) magnification.

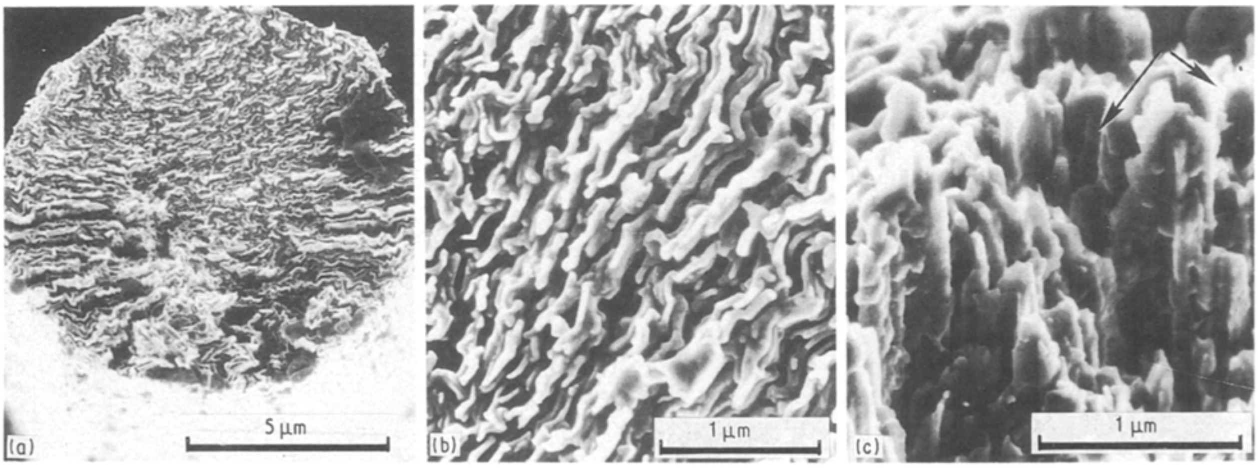

Figure 13 Scanning electron micrographs of P-100 fibre at (a) low and (b) high magnification. (c) Side view.

$L_a(90)$ value measured from WAXS for P-100 fibre is 80 nm. As seen from the view of the longitudinal section in Fig. 13c, the length of the graphitic sheets along the fibre axis is much larger. Also, Fig. 13c is taken from that part of the fibre which shows almost 90° bends in the graphitic sheets as indicated by the arrows. A stereo view of a section P-100 fibre is shown in Fig. 14.

Low- and high-resolution electron micrographs of pitch-based E-105 carbon fibre are shown in Fig. 15 for comparison with P-100 fibre. Like P-100, E-105 also shows well-developed sheet-like character. The sheets in E-105 appear much wider and thinner than in P-100. The thickness of most of the sheets is in the 10–15 nm range, and as is the case with P-100, this value matches the L_c value of this fibre. The stacking of sheets in E-105 appears to be quite good as is seen in Fig. 15b. The main difference between the two fibres is in the sheet width, which appears to be at least an order of magnitude greater in E-105. The sheet structure in the lower modulus E-35 pitch-based fibre is also remarkably well developed. In the pitch-based carbon fibres, other types of morphologies have also been reported. One example of a morphology different from those reported here, is for the pitch-based fibre from Idemitsu Co. In this fibre, sheet like morphology is interspersed with continuous structure. In terms of properties the knot strength and loop strength of this fibre were reported to be significantly higher than those of the other pitch-based carbon fibres [52].

HRSEM micrographs of three PAN-based carbon fibres are shown in Figs 16 and 17. High-resolution views of the transverse sections of T-40 and M-60J fibres (Fig. 16) do not show the development of sheet-like morphology; instead, these fibres exhibit a particulate morphology. Similar particulate morphology was reported for AS-4 and T-300 fibres [19]. The morphology of T-40 fibre appears to be quite inhomogeneous. Careful examination of Fig. 16a reveals the existence of some very small particles of about 20 nm size. In some places these particles appear to be part of a bigger structure. To our knowledge, such inhomogeneous morphological character for these fibres has not been previously reported. The smallest particle size (20 nm) is an order of magnitude larger than the crystallite sizes (L_c and $L_a(0)$ are 1.8 and 3.0 nm, respectively) for this fibre.

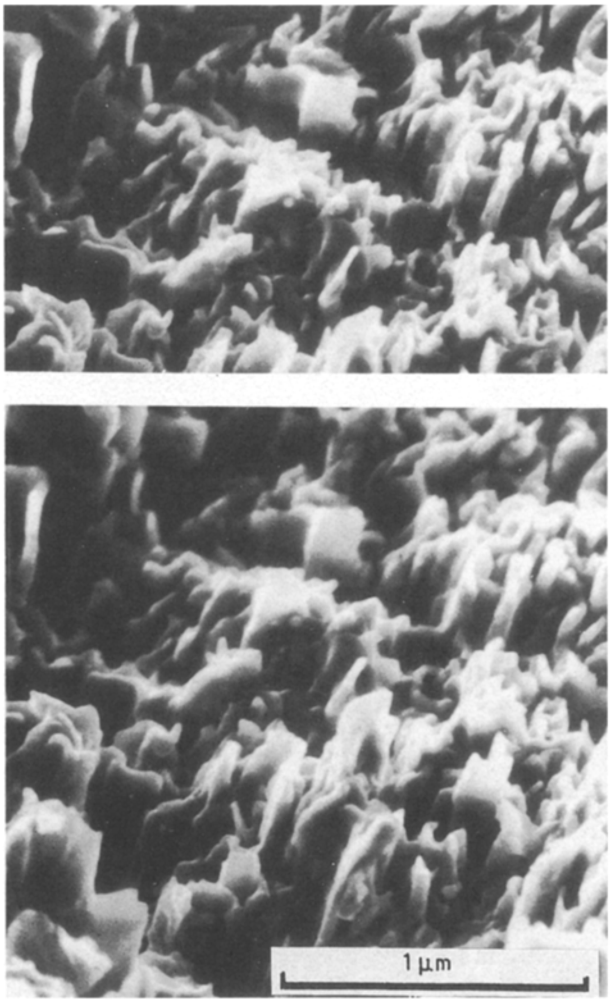

Figure 14 A stereo pair of P-100 fibre.

The particle size in M60J is approximately 40–50 nm, and this fibre also exhibits the absence of sheet-like character. Although the modulus of GY-70 is lower than that of M60J, sheet-like character is fully developed in GY-70 (Fig. 17) and not in M60J. Both fibres, however, show three-dimensional order. Another point to be mentioned here is that P-25 fibre has a sheet-like structure even though three-dimensional crystallinity is not observed, while M60J does not have sheet-like structure, and yet exhibits three-dimensional order in WAXS. This indicates that the development of a sheet-like structure and of three-dimensional crystalline order in carbon fibres are independent of each other, as either one could exist without the other. Good agreement is observed between the sheet thickness and crystallite size L_c in GY-70 fibre, both having values of about 15 nm. The three fibres where the sheet thickness matches the value of L_c are P-100, E-105, and GY-70. These three fibres are the ones where both three-dimensional crystalline order and sheet-like character are observed, indicating crystalline order in the L_c direction throughout the thickness of the fibril, the thickness of the fibril being observed using HRSEM.

It has been noted that the modulus of most carbon fibres decreases after outer layers of the fibres are removed [53], indicating that the orientation of graphitic sheets is higher on the surface than in the interior of a carbon fibre. Fig. 17 shows an area of fibre surrounding an internal defect (or macrovoid) in GY-70. The waviness in the graphite sheets around the void is significantly lower than in the rest of the specimen. This provides visual proof of the straightening of the graphitic sheets at a free surface. This implies that the fibres with a high surface area/volume ratio will have a larger percentage of straight sheets, influencing properties such as electrical and thermal

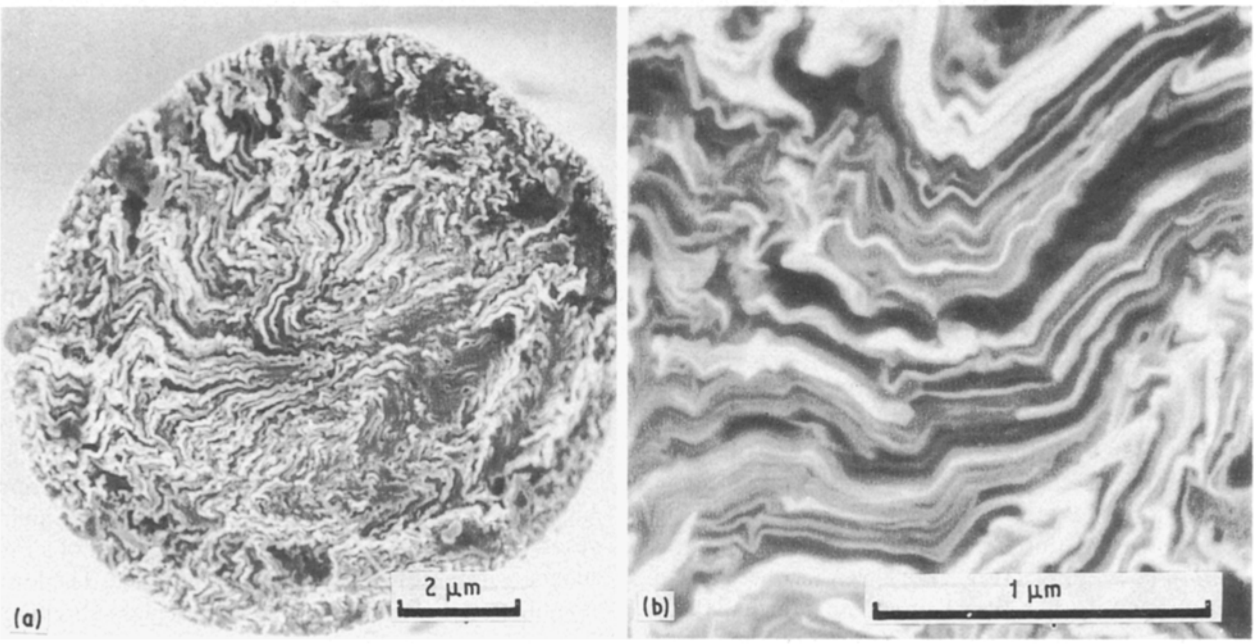

Figure 15 Scanning electron micrographs of pitch-based E-105 fibre: (a) low and (b) high magnification.

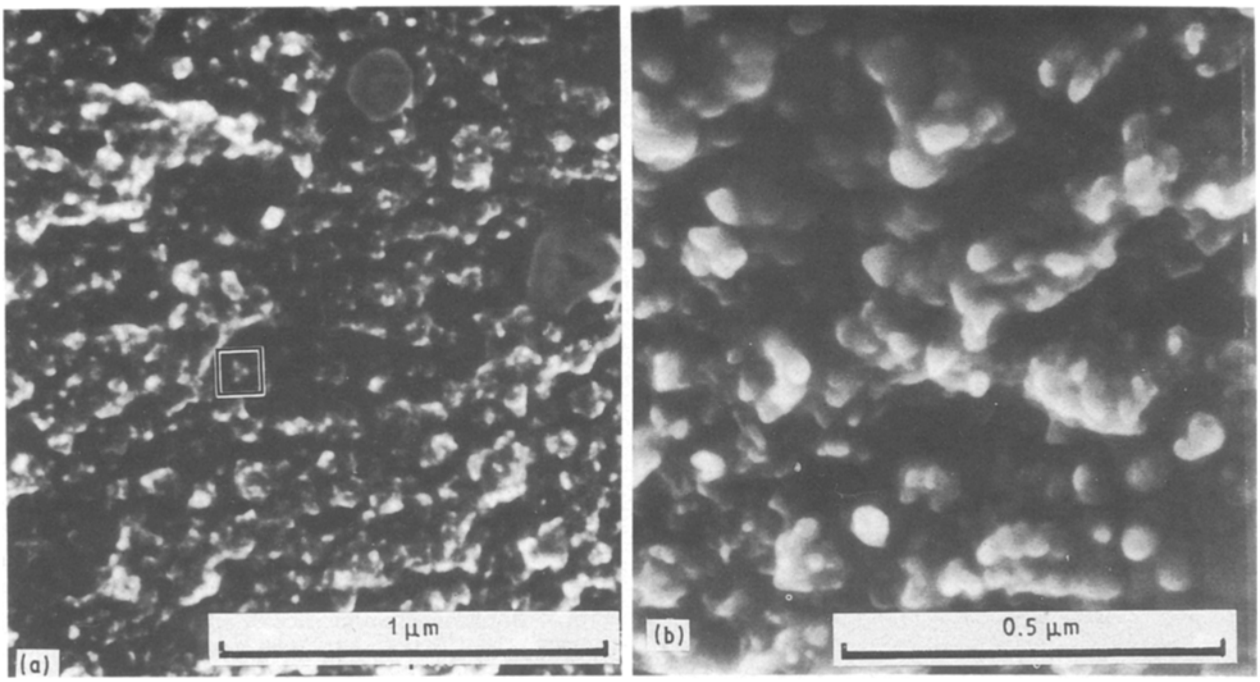

Figure 16 Scanning electron micrographs of PAN-based (a) T-40 and (b) M-60J fibres.

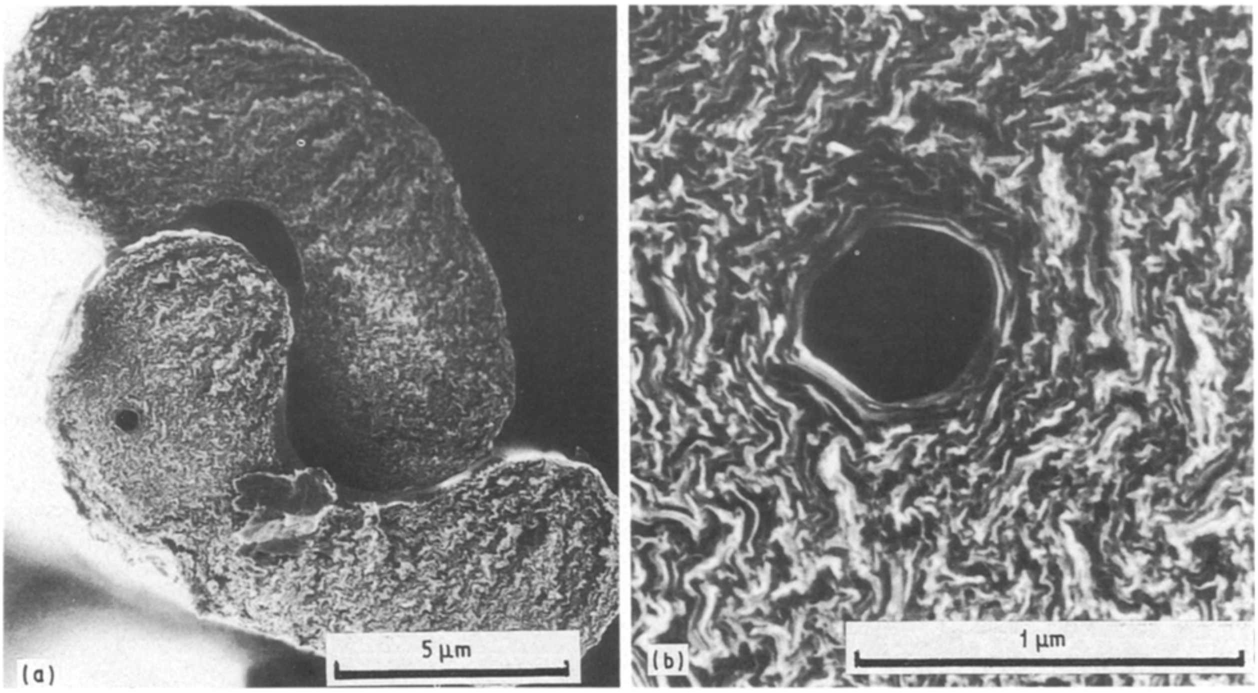

Figure 17 Scanning electron micrograph of PAN-based GY-70 fibre at (a) low and (b) high magnification.

conductivities. A hollow fibre has a larger surface area, and therefore a greater fraction of straight graphitic sheets than a solid fibre of identical cross-section.

Low- and high-resolution electron micrographs of the rayon-based T-75 carbon fibre are shown in Fig. 18. Pitch- and PAN-based fibres reported in this paper were either circular or kidney-shaped. The rayon-based fibre in Fig. 18a has an irregular shape. The morphology of this fibre as observed from high-resolution micrographs (Fig. 18b) is neither sheet-like, as in the case of pitch-based fibres, nor particulate, as observed in most PAN-based fibres, even though the low-resolution photograph in Fig. 18b at first seems to indicate a particulate structure. The morphology appears to be like snow flakes. The transverse dimensions of these snow flake like entities are in the 50–100 nm range. In many places these snow flakes appear to merge with one another. Longitudinally these snowflakes are likely to be in the form of fibrils.

The glass fibre micrographs in Fig. 19 at low and high magnification are given for comparison of high-resolution carbon fibre morphology with that of a homogeneous, non-fibrillar, isotropic material. The low-magnification photograph is typical of glass fibre fracture with river markings radiating from a mirror zone at the fibre surface. The fracture surface is somewhat

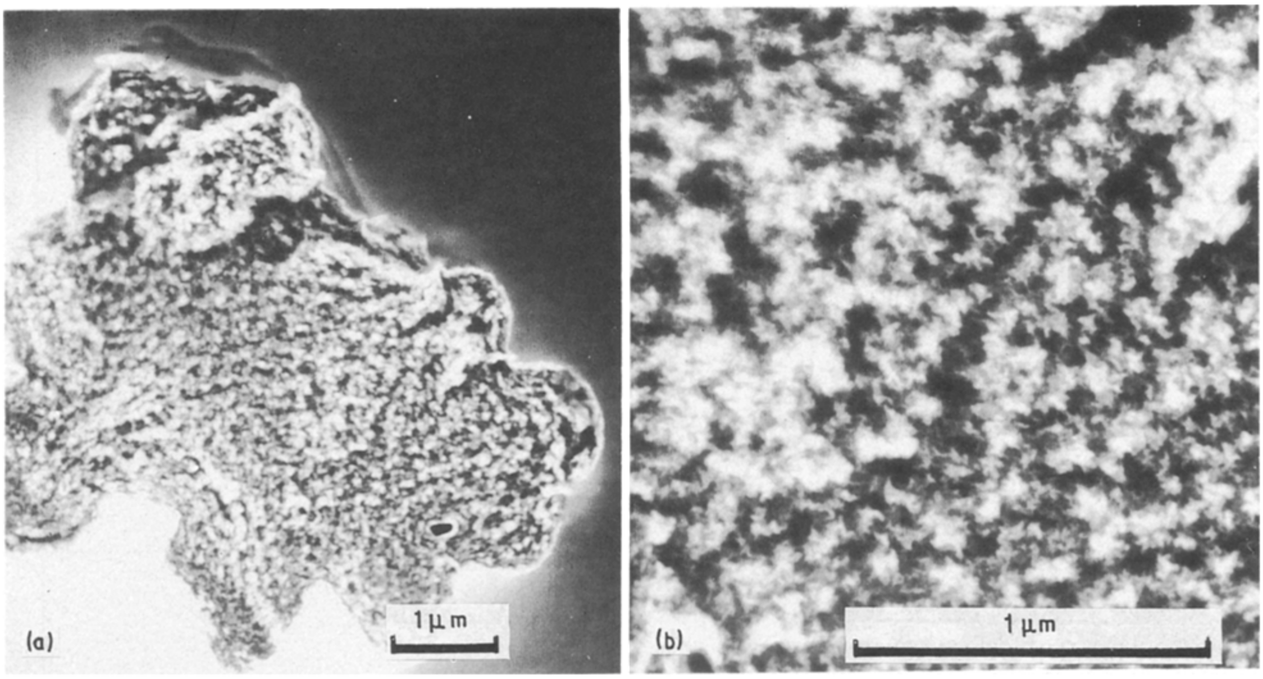

Figure 18 Scanning electron micrograph of rayon-based T-75 fibre at (a) low and (b) high magnification.

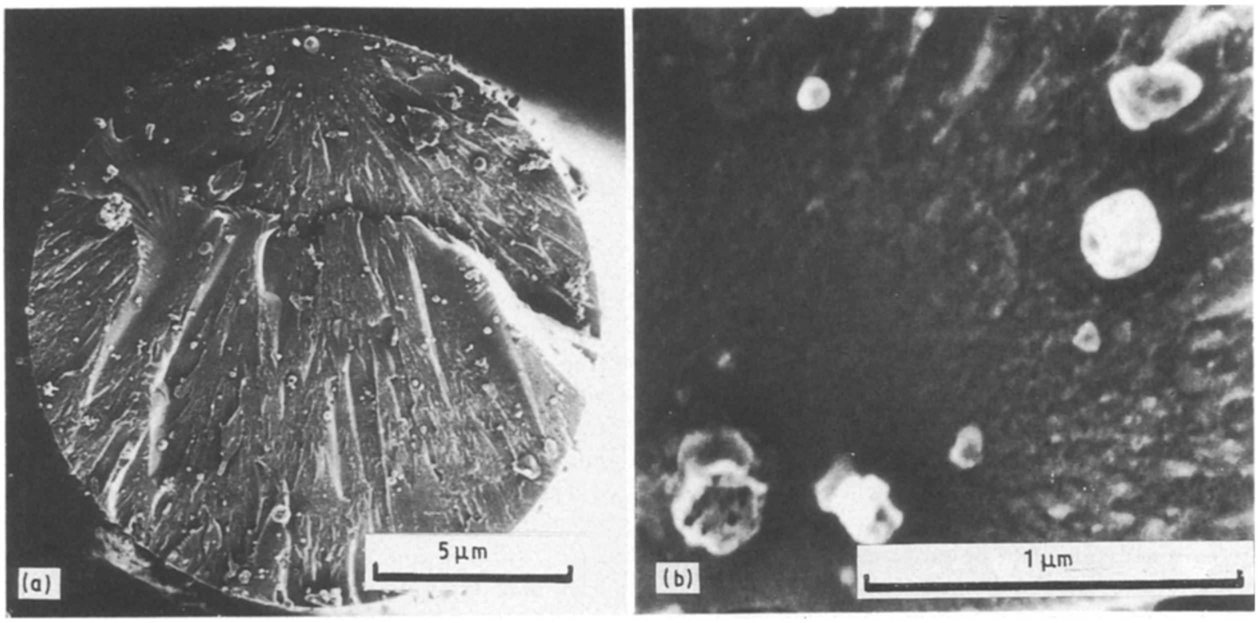

Figure 19 Scanning electron micrographs of E-glass fibres at (a) low and (b) high magnification.

uneven, with particles sitting on the surface, which may be impurities or dust. A high-magnification view indicates a fairly homogeneous surface; however, some particulate structure is observed. This structure is quite different from the particulate or sheet-like structure observed in carbon fibres.

A schematic representation of nitrogen release in the processing of carbon fibres is shown in Fig. 20 [54], where nitrogen exists at the edges of the graphitic planes. According to this model when the nitrogen content of the fibre is 3.8%, as is the case in T-40, then assuming a homogeneous distribution, each graphitic plane would be about 4 nm wide. The $L_a(0)$ value for the fibre is 3.0 nm. The graphitic width predicted on the basis of this nitrogen release model is of the same order of magnitude as $L_a(0)$. T-300, T-40, and T-50

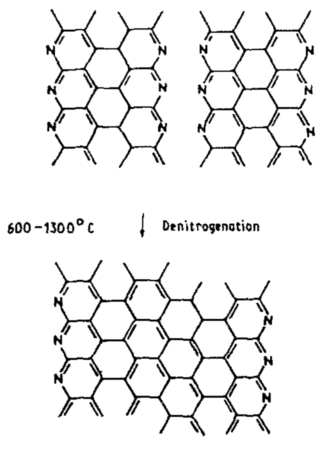

Figure 20 Schematic representation of carbon fibre preparation from PAN [20].

fibres are listed in order of decreasing nitrogen content. The decrease in nitrogen content is associated with an appropriate increase in $L_a(0)$. However, considering the inhomogeneous structure of T-40, it may be that evolution of nitrogen and hence the formation of a graphitic structure is through a nucleation and growth mechanism. If this is the case, then areas where graphitization has started will have lower concentration of nitrogen than the surroundings. Whether or not the inhomogeneity in Fig. 16b is of this nature, is yet to be determined.

3.3. Mechanical properties

The compressive strength of carbon fibres can be understood in terms of the following parameters: (i) bond energies (the carbon–carbon bond in the graphitic plane), (ii) compression of individual graphitic planes, (iii) compression of a group of graphitic planes or a single crystal, (iv) compression of a group of graphitic planes with defects (bends, twists, and misorientation) and vacancies (missing carbon atoms in the graphitic plane), and (v) compression of the fibre, comprising of a large number of groups of graphitic planes (fibrils) with varying degrees of defects, vacancies, and sizes.

If failure occurs at the C–C bond level, then the compressive strength should be governed by the bond energy. Based on the C–C bond breaking energy, the strength for this bond is about 20 GPa. The reported compressive strength of diamond is 14 GPa [55] which is very close to the value calculated from the carbon–carbon bond energy, suggesting that the compression failure in diamond is mainly due to the breakage of the C–C bond. If failure occurs at the level of the individual graphitic planes then the compressive strength may depend on the dimensions of the plane. Next under consideration is the compression of a group of perfect graphitic planes or a graphite single crystal. Single-crystal graphite has a compressive strength of 105 MPa [56] and is believed to fail in the twinning mode. In a carbon fibre, the compressive strength is expected to be governed by one or more of the above factors. In addition, lattice vacancies, defects, orientation, and voids also influence this property.

A plot of fibre tensile modulus as a function of orientation parameter Z is given in Fig. 21. This plot shows the generally accepted relationship of an increase in modulus with increasing orientation, with some scatter in the low-modulus range. Fourdeux *et al.* [57] demonstrated that the tensile modulus, corrected for porosity, correlates well with the orientation parameter, q. The relationship between E and q followed a model based on unwrinkling of fibrils. This work was done on a large number of rayon-based fibres and included one pitch-based and two PAN-based fibres. We have also calculated the orientation parameter q, and the modulus correlation with q is no better than it is with Z. Our modulus values have not been corrected for porosity. However, for the same fibre modulus, PAN-based fibres generally have a lower density than pitch-based fibres. The correction for porosity would therefore increase the observed difference in modulus between the two fibre types (Fig. 21) for the same orientation parameter. Other workers have also reported that the relationship between fibre modulus and orientation distribution is not unique [58, 59].

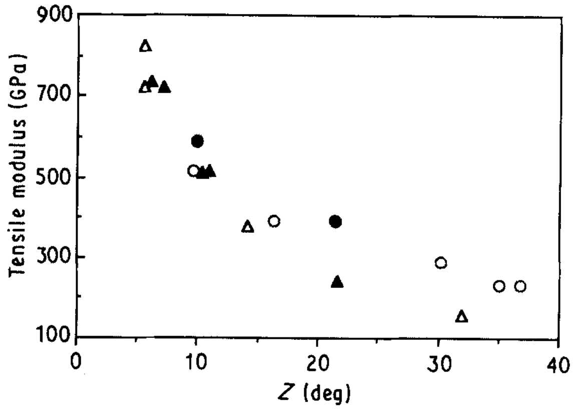

Figure 21 Fibre tensile modulus as a function of orientation parameter, Z. (△) Pitch-1, (▲) pitch-2, (○) PAN-1, (●) PAN-2.

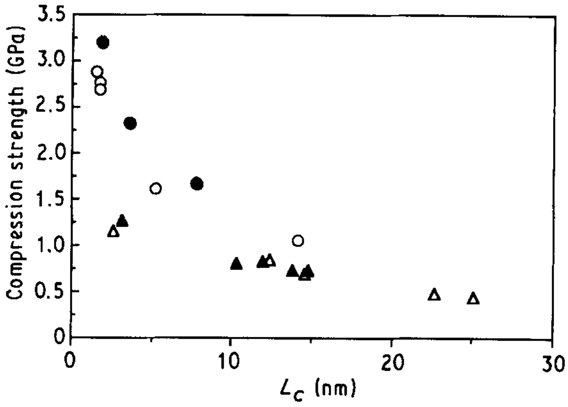

Figure 22 Fibre compressive strength as a function of L_c. For key, see Fig. 21.

The relationships between fibre compressive strength and various structural parameters such as L_c, L_c/L_a, $d(0\,0,2)$, void content, orientation, and density have been reported earlier [1, 8, 9, 39]. The general trends observed were a decrease in compressive strength with increasing L_c, orientation, density, and with decreasing $d(0\,0,2)$, and void content. For those pitch-based fibres which exhibited three-dimensional crystallinity, a linear decrease in compressive strength was noted with increasing crystallite aspect ratio, L_a/L_c [9, 39]. A correlation between these two parameters, however, was not observed, for all carbon fibres. Other structural parameters which exhibited correlations with fibre compressive strength did so usually only within fibres of a particular precursor (pitch or PAN).

A plot of fibre compressive strength versus L_c is shown in Fig. 22. These results show a good correlation for all the pitch-based fibres, while for the same L_c compressive strength of PAN-2 is higher than that of the PAN-1 fibres. The results for low-modulus pitch-based fibres (P-25 and E-35), and high-modulus PAN-based fibres (M60J and GY-70) deviate from a

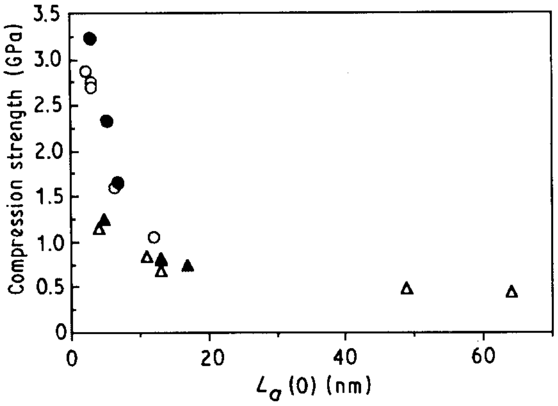

Figure 23 Fibre compressive strength as a function of $L_a(0)$. For key, see Fig. 21.

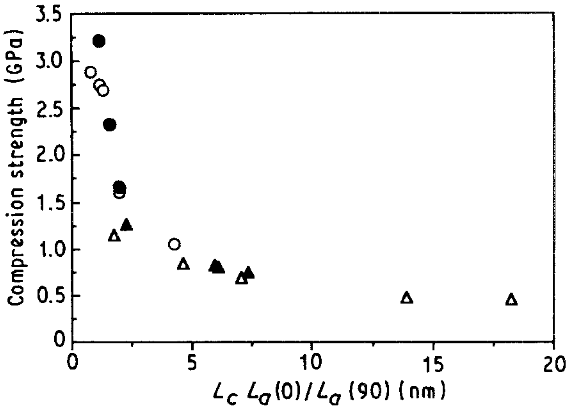

Figure 24 Fibre compressive strength as a function of crystalline cross-section per unit length. For key, see Fig. 21.

common curve which may be drawn through the data. The deviations for P-25 and E-35 are significant, and undoubtedly beyond the measurement errors in either compressive strength or L_c. Although of all the structural parameters previously mentioned L_c shows the best correlation with compressive strength, and it is conceivable that larger crystals are more susceptible to buckling or twinning, the data in Fig. 22 suggests that the differences in compressive strength between PAN-based fibres (such as T-300 and AS4) and pitch-based fibres (such as E-35 and P-25) cannot be explained on the basis of the difference in L_c alone.

The fibre compressive strength as a function of L_a (0) is shown in Fig. 23. The data for both PAN-1 and PAN-2 fall on the same line and overall the correlation with $L_a(0)$ is better than with L_c. This may suggest that $L_a(0)$ influences the compressive strength more than L_c. The graphitic plane width in the direction of $L_a(0)$ is likely related to the nitrogen content in the case of PAN-based carbon fibres (see Fig. 20 for the mechanism). The presence of nitrogen may prevent the development of sheet-like morphology in the lower-modulus carbon fibres. The width of the graphitic sheets and the crystallite size may also be governed by variations in precursor composition and in processing conditions. For example, the addition of a second phase may prevent the growth of the crystallites or graphitic sheets in the L_c and $L_a(0)$ direction. In the case of pitch-based fibres, the sheet-like character is visible even in the low-modulus P-25 and E-35 fibres. Because of the waviness of these sheets the $L_a(0)$ measured in low-modulus pitch-based fibres will be lower than the $L_a(0)$ in the low-modulus PAN fibres, where the sheet-like character is not yet developed. The waviness of the sheets is not likely to affect the L_c measurement.

The compressive strength as a function of crystallite cross-sectional area per unit length (crystal anisotropy) is plotted in Fig. 24 for all the carbon fibres studied. Crystal anisotropy, as measured by $L_c^* L_a(0)/L_a(90)$, provides the best correlation thus far with carbon fibre compressive strength. The data for compressive strength versus crystal anisotropy of pitch-1, pitch-2, PAN-1, and PAN-2 fall on the same plot, with small deviation. The deviations between two series of pitch and PAN fibres have been eliminated, and the deviations for P-25 and E-35 have been significantly reduced.

Compressive strength decreases rapidly with crystal anisotropy, when $L_a(0)$ is less than about 10 nm (or crystalline anisotropy parameter is less than about 3 nm). Above these values the compressive strength decreases more slowly. This may indicate two different failure mechanisms in compression. In the fibres with small crystallite size, fibrillar buckling may predominate. In fibres with larger crystallite size, with well-developed three-dimensional crystalline order, shearing or twinning may be the mechanism which initiates compression failure. P-25 and E-35 may also fail in the shear or twinning mode because of well-developed sheet-like character, even though these fibres do not exhibit three-dimensional crystalline order. One factor which may be important in controlling compression behaviour is the relative amounts of well-developed crystalline regions and paracrystalline and disordered region. The relative amounts of the two regions have not yet been determined.

From these results it is apparent that the compressive strength decreases with increased modulus not so much because of the increased orientation, but because of the increased crystallite size. If the fibre orientation could be increased while limiting the increase in L_c and $L_a(0)$, it should then be possible to produce high-modulus carbon fibres without sacrificing compressive strength. The differences between pitch-1 and pitch-2 fibres and PAN-1 and PAN-2 fibres indicate that some control on crystallite size growth is possible.

4. Conclusions

1. For carbon fibres from a given precursor, compressive strength decreases with increase in tensile modulus. However, by influencing the structure and morphology the compressive strength can be increased for a given modulus. This is true for fibres both from PAN and pitch precursors.

2. For a given modulus, the compressive strength of PAN-based carbon fibres is higher than the compressive strength of either pitch-based or rayon-based carbon fibres.

3. The crystallite size, L_c, ranges from 1.5 nm in low-modulus PAN-based fibres to 25 nm in high-modulus pitch-based fibres. The corresponding values

for $L_a(0)$ and $L_a(90)$ range from 2–64 nm and 4–88 nm, respectively. The (0 0, 2) d-spacings for these fibres range from 0.3376–0.344 nm. This range is somewhat narrower than previously reported, where corrections for the Lorentz and structure factors were not applied. The azimuthal full-width at half-intensity maxima (FWHM) for the (0 0, 2) reflection reported as Z, is in the range of 5°–37°.

4. High-resolution scanning electron microscopy (HRSEM) indicates sheet-like morphology in all pitch-based fibres, even in low-modulus P-25 where no three-dimensional order is observed from WAXS. With an increase in fibre modulus the sheet boundaries become more defined. In most PAN-based fibres a particulate rather than sheet-like morphology was observed. The particulate morphology was present even in high-modulus PAN-based M60J carbon fibre, in which three-dimensional order is observed from WAXS. These results indicate that sheet-like morphology does not necessarily imply a three-dimensional order (e.g. P-25). On the other hand, a fibre with particulate morphology can display three-dimensional order (e.g. M60J). The PAN-based GY-70 shows well-developed graphitic sheets and three-dimensional order.

5. Considering the various structural parameters and morphology of the fibre, the variations in crystallite size L_c and $L_a(0)$, the crystallite anisotropy $L_cL_a(0)/L_a(90)$, and the development of a sheet-like structure in the fibre seem to be the factors responsible for the significant compressive strength differences in various fibres. Other crystallite dimensions also have some influence.

6. The fibre compressive strength can be improved for a given modulus if the desired (0 0, 2) orientation in the fibre can be achieved with smaller crystallite size. Controlling the development of sheet-like character is also likely to help. The compression failure mechanism in different fibres may be different, and is yet to be studied.

Acknowledgements

This work was supported under Air Force Contract number F33615-87-C-5239 and a grant from the Air Force Office of Scientific Research (AFOSR-91-0194).

References

1. S. KUMAR and T. E. HELMINIAK, in "The Materials Science and Engineering of Rigid Rod Polymers", edited by W. W. Adams, R. K. Eby and D. E. McLemore Materials Research Society Symposium Proceedings 134 (MRS, Pittsburgh, 1989) p. 363.
2. J. H. GREENWOOD and P. G. ROSE, *J. Mater. Sci.* **9** (1974) 1809.
3. H. M. HAWTHORNE and E. TEGHTSOONIAN, *ibid.* **10** (1975) 41.
4. H. T. HAHN and M. M. SOHI, *Compos. Sci. Technol.* **27** (1986) 25.
5. T. NORITA, A. KITANO and K. NOGUCHI, in "Proceedings of the IVth Japan–US Conference on Composite Materials" (Technomic, 1988).
6. H. T. HAHN and J. G. WILLIAMS, NASA technical memorandum 85834, August 1984.
7. H. T. HAHN, M. SOHI and S. MOON, NASA contract report 3988, June 1986.
8. S. KUMAR, W. W. ADAMS and T. E. HELMINIAK, *J. Reinf. Plast.* **7** (1988) 108.
9. A. CRASTO and D. P. ANDERSON, *Proc. Amer. Soc. Comp.* **5** (1990) 809.
10. Y. MATSUHISA, M. WASHIYAMA, T. HIRAMATSU, H. FUJINO and G. KATAGIRI, "Proceedings of the 20th Bienniel Carbon Conference" Santa Barbara (1991) p. 226.
11. J. G. DaSILVA and D. J. JOHNSON, *J. Mater. Sci.* **19** (1984) 3201.
12. W. R. JONES and J.W. JOHNSON, *Carbon* **9** (1991) 645.
13. W. S. WILLIAMS, D. A. STEFFENS and R. BACON, *J. Appl. Phys.* **41** (1970) 4893.
14. E. TSUSHIMA, in "34th International, SAMPE Symposium", May 1989, p. 2042.
15. S. FIDAN, Air Force Institute of Technology, MS Thesis, AFIT-GAE-AA-88D-14 (1988).
16. K. KUBOMURA and N. TSUJI, in "36th SAMPE International Symposium Proceedings" (1991).
17. A. CRASTO and R. KIM, *ibid.* (1991) p. 1649.
18. S. KAWABATA, *J. Textile Inst.* **81** (1990) 432.
19. D. L. VEZIE and W. W. ADAMS, *J. Mater Sci. Lett.* **9** (1990) 883.
20. M. ENDO, *J. Mater. Sci.* **23** (1988) 598.
21. T. NORITA, Toray, private communication.
22. S. KUMAR and R. KIM, unpublished results.
23. A. G. EVANS and W. F. ADLER, *Acta Metall.* **26** (1978).
24. SAMPE reference for M60J, and M40J
25. D. SINCLAIR, *J. Appl. Phys.* **21** (1950) 380.
26. S. J. DeTERESA, R. S. PORTER and R. J. FARRIS, *J. Mater. Sci.* **23** (1988) 1886.
27. S. ALLEN, *ibid.* **22** (1987) 853.
28. A. S. CRASTO and R. Y. KIM, *SAMPE Q.* April (1991) 29.
29. S. J. DeTERESA, in "14th Annual Mechanics of Composites Review" Dayton, OH (1989).
30. A. CRASTO and S. KUMAR, in "35th International SAMPE Symposium" (1990) p. 318.
31. S. KUMAR, *ibid.* 2224.
32. C. HERINCKX, R. PERRET and W. RULAND, *Nature* **220** (1968) 63.
33. *Idem., Carbon* **10** (1972) 711.
34. P. EHRBURGER, J. J. HERQUE and J. B. DONNET, in "5th London International Carbon and Graphite Conference, 1", (Society Industries, London, 1978).
35. F. L. VOGEL, *Carbon* **14** (1976) 175.
36. M. S. DRESSELHAUS, G. DRESSELHAUS, K. SUGIHARA, I. L. SPAIN and H. A. GOLDBERG, "Graphite Fibres and Filament" (Springer, New York, 1988) p. 244.
37. D. A. JAWORSKE, R. D. VANNUCCI and R. ZINOLABEDINI, *J. Compos. Mater.* **21** (1987) 580.
38. D. A. JAWORSKE, J. R. GAIER, C. C. HUNG and B. A. BANKS, *SAMPE Q.* **18** (1986) 9.
39. D. P. ANDERSON and S. KUMAR, in "Annual Technical Conference Society of Plastics Engineers", May 1990, p. 1248.
40. M. INAGAKI, *J. Mater. Res.* **4** (1989) 1560.
41. D. P. ANDERSON, WRDC-TR-90-4137 (1991).
42. P. M. DEWOLFF, *J. Polym. Sci.* **60** (1962) S34.
43. P. SCHERRER, *Gottinger Nachrichten* **2** (1918) 98.
44. R. HOSEMANN, *Z. Physik* **128** (1950) 1.
45. *Idem, ibid.* **128** (1950) 464.
46. D. R. BUCHANAN, R. I. McCULLOUGH and R. L. MILLER, *Acta Crystallogr.* **20** (1966) 922.
47. W. RULAND, *ibid.* **22** (1967) 615.
48. *Idem*, in "Chemistry and Physics of Carbon", edited by P. L. Walker Jr, (Marcel Dekker, New York, 1968) 1.
49. B. E. WARREN and P. BODENSTEIN, *Acta Crystallogr.* **20** (1966) 602.
50. B. E. WARREN, *Phys. Rev.* **59** (1941) 693.
51. G. NORTHOLT and H. A. STUUT, *J. Polym. Sci. Polym. Phys. Ed.* **16** (1978) 939.
52. Idemitsu Fiber Bulletin Tokyo-100, Japan.
53. K. J. CHEN and R. J. DIEFENDORF, in "Progress in

Science and Engineering of Composites", edited by T. Hayashi, K. Kawata and S. Umekawa, ICCM-IV, Tokyo (1982) 97.
54. P. J. GOODHEW, A. J. CLARKE and J. E. BAILEY, *Mater. Sci. Engng* **17** (1975) 3.
55. M. G. NORTHOLT, *J. Mater. Sci.* **16** (1981) 2025,
56. W. H. SMITH and D. H. LEEDS, in "Modern Materials—Advances in Development and Applications", Vol. 7, edited by B. W. Gonser (Academic Press, 1970) p. 166.
57. A. FOURDEUX, R. PERRET and W. RULAND, *J. Appl. Crystallogr.* **1** (1968) 252.
58. S. CHWASTIAK and R. BACON, *Polym. Prep.* (*ACS*) **22**(2) August (1981) 222.
59. R. J. DIEFENDORF and E. TOKARSKY, *Polym. Engr. Sci.* **15** (1975) 1975.

Received 18 October 1991
and accepted 24 March 1992